



Title	Role of the Rossby Waves in the Broadening of an Eastward Jet
Author(s)	Mizuta, Genta
Citation	Journal of Physical Oceanography, 42(3), 476-494 https://doi.org/10.1175/JPO-D-11-070.1
Issue Date	2012-03
Doc URL	http://hdl.handle.net/2115/49936
Rights	© Copyright 2012 American Meteorological Society (AMS). Permission to use figures, tables, and brief excerpts from this work in scientific and educational works is hereby granted provided that the source is acknowledged. Any use of material in this work that is determined to be "fair use" under Section 107 of the U.S. Copyright Act or that satisfies the conditions specified in Section 108 of the U.S. Copyright Act (17 USC § 108, as revised by P.L. 94-553) does not require the AMS' s permission. Republication, systematic reproduction, posting in electronic form, such as on a web site or in a searchable database, or other uses of this material, except as exempted by the above statement, requires written permission or a license from the AMS. Additional details are provided in the AMS Copyright Policy, available on the AMS Web site located at (http://www.ametsoc.org/) or from the AMS at 617-227-2425 or copyright@ametsoc.org .
Type	article
File Information	JPO42-3_476-494.pdf



[Instructions for use](#)

Role of the Rossby Waves in the Broadening of an Eastward Jet

GENTA MIZUTA

Graduate School of Environmental Earth Science, Hokkaido University, Sapporo, Japan

(Manuscript received 31 March 2011, in final form 15 October 2011)

ABSTRACT

To investigate the effect of the Rossby waves on an eastward jet such as the Kuroshio or Gulf Stream Extensions, a series of numerical experiments is conducted using a primitive equation model. In these experiments, an inflow and an outflow imposed on the western and eastern boundaries drive an unstable narrow jet and a broad interior flow in the western and eastern regions of the model domain, respectively. The barotropic Rossby waves are radiated from the transient region between the two regions. The eddy potential vorticity flux by the waves tends to compensate for the difference in the mean potential vorticity along mean streamlines between both sides of the transient region. Instability of the jet is insufficient for this compensation and weakens the mean potential vorticity gradient too much. Moreover, as the potential vorticity of the outflow is increased, the Rossby waves are intensified in order to compensate for the increase in the difference in the mean potential vorticity. These features strongly suggest that the Rossby waves are substantial in matching a jet with an interior flow. The speed of the waves and properties of eddies in recirculations of the jet are consistent with a two-layer analytic model, which indicates that the Rossby waves are radiated from eddies in recirculations. These eddies as well as the Rossby waves increase in amplitude with the transport of the recirculation near the surface presumably because of mean advection. Therefore, the mean potential vorticity of the interior flow, the intensity of the Rossby waves, and the transport of the recirculation change consistently with one another.

1. Introduction

The Kuroshio and Gulf Stream systems separated from the coast in the northern half of the subtropical gyre are accompanied by high eddy activity (Ducet and Taron 2001), suggesting that instability, the interaction between eddies, and rectification of eddy energy occur in these regions. The nonlinearity of this western boundary current extension (WBCE) is considered to be integral, for example, to the driving of the recirculation of the Kuroshio and Gulf Stream systems (Holland and Rhines 1980). The WBCE is broadened and matched to the weak flow in the ocean interior, passing through this turbulent region.

Both observations (Thompson 1977; Hogg 1981) and numerical experiments (Holland 1978; Jayne et al. 1996) indicate that the radiation of the Rossby waves is a common feature in the WBCE region. Rectification of Rossby wave energy has been proposed as a mechanism for the

maintenance of the northern recirculation gyre of the Gulf Stream (Hogg 1988; Malanotte-Rizzoli et al. 1995; Mizuta and Hogg 2004; Waterman and Jayne 2011). However, the precise role of the Rossby waves on the mean flow in the WBCE region has not yet been clarified.

In the theory of the wind-driven circulation, the western boundary current is required in order to supplement the Sverdrup interior flow, which cannot satisfy the boundary condition by itself (Stommel 1948; Munk 1950). Although the viscous boundary layer that is confined near the western boundary exists at all latitudes, this is not exactly the case for the inertial boundary layer at latitudes where the interior flow is eastward (Pedlosky 1987). The WBCE and recirculation are typically located at these latitudes between the western boundary and the interior region.

The low (high) potential vorticity of water advected from the low (high) latitudes by the western boundary current is adjusted to the same value as that of the ocean interior, when this water enters the interior through the WBCE region. For laminar flow with the no-slip boundary condition, the adjustment occurs because of horizontal viscosity while water circulates in the recirculation

Corresponding author address: Genta Mizuta, Graduate School of Environmental Earth Science, Hokkaido University, N10W5, Sapporo 060-0810, Japan.
E-mail: mizuta@ees.hokudai.ac.jp

gyre and stationary meanders (Cessi et al. 1990; Cessi 1991). Eddy motions are essential for the adjustment of turbulent flow (e.g., Fox-Kemper and Pedlosky 2004). However, the precise mechanism of the adjustment has not yet been fully examined.

The entire adjustment process, including the redistribution of the potential vorticity by eddies, should depend on the distribution of the interior flow, to which the western boundary current is matched, unless the WBCE region is extended across the basin, reaching the eastern boundary. Recent analysis of data from satellite altimetry and an ocean general circulation model indicate that the decadal variability of the recirculation and eddy activities in the Kuroshio Extension is correlated with that of the large-scale interior flow excited by the wind stress in the North Pacific (Taguchi et al. 2005, 2007; Qiu and Chen 2005, 2010). Qiu and Chen (2005) identified the contracted and elongated modes, which are characterized by small and large zonal extent of the recirculation, respectively, in the decadal variability of the Kuroshio Extension. They showed that the shift between the two modes occurs when the baroclinic Rossby waves excited by the wind stress in the downstream region of the Kuroshio Extension arrives at the recirculation. These changes suggest the existence of an adjustment process of the Kuroshio Extension, although the wind stress in the real ocean changes in both strength and pattern, making a simple interpretation difficult.

The adjustment of the potential vorticity across the WBCE region is accompanied with the nonlinear evolution of the large-scale flow, mesoscale eddies, and Rossby waves and the interaction between them. To better understand the basic processes of this complex adjustment of the potential vorticity, the present study examines results of an idealized numerical experiment. This adjustment process is the fundamental part of the wind-driven circulation, and the understanding of this process may contribute to the study of the decadal variability of the WBCE.

The primary goal of the present study is to examine the role of the Rossby waves on the adjustment of the potential vorticity across the WBCE region. For this purpose, numerical experiments are conducted, in which a narrow unstable inflow and a broad stable outflow were imposed on the western and eastern boundaries of a rectangular basin, respectively. The inflow and outflow correspond to the WBCE near the coast and the western part of the interior flow, respectively. The distribution of the outflow on the eastern boundary was changed in order to examine how the circulation near the western boundary of the model domain adjusts to the change. This change of the outflow corresponds to the change of the wind stress curl in latitudes where the interior flow is

eastward in the real ocean. We focus on the dependence of the experimental results on the distribution of the potential vorticity of the outflow. Because the distribution of the inflow was fixed, the total transport of the outflow was constant.

Moreover, the radiation mechanism of the Rossby waves from the WBCE has not yet been fully investigated. Talley (1983a,b) examined the radiation of the Rossby waves on the basis of the linear instability of a zonal jet. In her analysis, the phase velocity of the perturbation inside an eastward jet matches that of the westward-propagating Rossby waves outside the jet when the jet is flanked by westward flows, although, from the semicircle theorem with the nonzero beta effect, the westward flows are not the necessary condition for the perturbation to propagate westward. Hogg (1988) showed that the (neutral) Rossby waves can be radiated from eastward-propagating meanders of the Gulf Stream. Because of the sporadically growing and spatially localized feature, the meanders have a westward-propagating component in the frequency–wavenumber domain. By examining the Rossby waves radiated from a jet and recirculation in numerical experiments, Mizuta (2009) showed that the zonal phase speed of the Rossby waves matches the speed of the westward recirculation. This feature of the zonal phase speed cannot be directly explained by studies by Talley (1983a,b) and Hogg (1988). He speculated that the Rossby waves are radiated from the eddies in the recirculation and analytically showed that the zonal speed of the perturbation matches the speed of the basic flow in an initial value problem. However, the distribution and speed of the eddies in the recirculation were not examined. The analytic solution was obtained in the barotropic model, and the effect of the stratification on the perturbation was not clear.

The second goal of the present study is to examine the radiation mechanism of the Rossby waves in the WBCE region. In the present study, numerical experiments are conducted in order to demonstrate that the intensity of the Rossby wave radiation depends on the distribution of the potential vorticity of the outflow. Then, the relationship of the eddies in the recirculation with the potential vorticity of the outflow and the Rossby waves are examined. An analytic solution in the two-layer model is also obtained.

The remainder of the present study is organized as follows: In the next section, the numerical model used in the present study and the experimental conditions are described. The effect of the Rossby waves on the mean flow is examined in section 3. The radiation mechanism of the Rossby waves is then discussed in section 4. The results obtained in these sections are summarized in section 5.

2. Model

The present study used the Regional Ocean Model System (ROMS; Haidvogel et al. 2000), which is a primitive equation model with Boussinesq and hydrostatic approximations. The model domain was a rectangle on the beta plane with a uniform bottom depth of $H_0 = 4000$ m. An inflow u_{in} and an outflow u_{out} , which are defined as

$$u_{\text{in}} = \frac{u_0 K(z)}{\cosh^2 \frac{y}{L_{\text{in}}}} \quad \text{and} \quad (1)$$

$$u_{\text{out}} = \frac{ru_0 K(z)}{\cosh^2 \frac{y}{L_{\text{out}}}}, \quad (2)$$

were imposed on the western and eastern boundaries, respectively, where

$$r = \frac{\int_{-Y/2}^{Y/2} \frac{dy}{\cosh^2 \frac{y}{L_{\text{in}}}}}{\int_{-Y/2}^{Y/2} \frac{dy}{\cosh^2 \frac{y}{L_{\text{out}}}}}. \quad (3)$$

Here, (x, y, z) are the zonal, meridional, and vertical coordinates, respectively, with the origin located at the middle of the western boundary at the surface. Both the inflow and outflow have a maximum of the zonal velocity at the middle of the boundary, with their transport being the same at each depth. The width of the inflow L_{in} was 30 km, which is roughly comparable to the instantaneous width of the Kuroshio (Imawaki et al. 1997). The amplitude of the inflow u_0 , the width of the outflow L_{out} , and the meridional dimension of the model domain Y will be discussed later. The vertical structure $K(z)$ of the inflow and outflow was

$$K(z) = \frac{1}{1-k} \left(e^{z/d_0} - ke^{z/d_1} \right), \quad (4)$$

where $d_0 = 750$ m, $d_1 = 200$ m, and $k = 0.133$. These coefficients and the stratification were determined based on the climatological values in the upstream part of the Kuroshio Extension in the *World Ocean Atlas 2001* (Boyer et al. 2002; Stephens et al. 2002). The temporal variability of the vertical structure of the Kuroshio is rather small, and the mean and the instantaneous structures of the transport averaged in the across-flow direction are similar to each other (Imawaki et al. 2001). The density of the inflow and outflow was the sum of the climatological stratification that is horizontally uniform

TABLE 1. Experimental conditions.

	$L_{\text{out}} L_{\text{in}}^{-1}$	Y (km)	u_0 (m s^{-1})	$j_{\text{out}} L_{\text{in}} u_0^{-1}$
N5	5	1280	0.4	0.45
N10	10	1280	0.4	0.56
Ninf	∞	1280	0.4	0.69
L20	20	1920	0.4	0.79
Linf	∞	1920	0.4	0.95
Sinf	∞	900	0.4	0.57
N10U8	10	1280	0.8	0.42
NinfU8	∞	1280	0.8	0.49
L15U8	15	1920	0.8	0.50
LinfU8	∞	1920	0.8	0.61

and the density that is in geostrophic balance with the zonal velocity prescribed at the boundaries. Here, because the density in the model does not depend on the salinity and pressure, the buoyancy frequency was fitted in the determination of the stratification. The first internal deformation radius by this stratification was ~ 30 km at the center of the model basin, where the Coriolis coefficient was $f_0 = 9 \times 10^{-5} \text{ s}^{-1}$, which is the value around 38°N . The planetary beta was $\beta = 2 \times 10^{-11} \text{ m}^{-1} \text{ s}^{-1}$. The zonal dimension of the model domain was $X = 5120$ km.

We examine how the mean flow, the intensity of the Rossby waves, and the distribution of eddy potential vorticity flux respond to the change in the potential vorticity of the outflow by conducting the experiments listed in Table 1. In these experiments, L_{out} changed from $5L_{\text{in}}$ in experiment N5 to infinity (i.e., the outflow was uniform in the meridional direction) in experiment Ninf. As a measure of the potential vorticity of the outflow, the present study adopted the normalized potential vorticity flux j_{out} through the northern half of the eastern boundary. Here, j_{out} is defined as

$$j_{\text{out}} = \frac{\int_A u q_1 H(y) dy dz}{\int_A u H(y) dy dz} \quad \text{and} \quad (5)$$

$$q_1 = \beta y + v_x - u_y + f_0 \left(\frac{b}{N^2} \right)_z, \quad (6)$$

where u (v) is the eastward (northward) velocity, q_1 is the deviation of the potential vorticity from f_0 , b is the buoyancy, N^2 is the buoyancy frequency, A is the area of the eastern boundary, and $H(y)$ is the Heaviside step function [i.e., $H(y) = 0$ and 1 in $y < 0$ and $y > 0$, respectively]. Thus, j_{out} corresponds to the mean potential vorticity weighted with u . The present study adopted the zonal velocity as the weight, because the potential vorticity, for example, at the point where $u = 0$ in A does not affect the matching between the inflow and outflow. Note that $u q_1$ is an odd function of y and that the numerator of

(5) becomes zero without $H(y)$. The value of j_{out} scaled with $u_0 L_{\text{in}}^{-1}$ is listed in Table 1. Within the range of L_{out} in Table 1, j_{out} increases with L_{out} because the planetary vorticity dominates in (6) (e.g., experiments N5, N10, and Ninf). The value of j_{out} decreases with increasing L_{out} for smaller values of L_{out} because of the relative vorticity, which is negative and positive in $y < 0$ and $y > 0$, respectively. For such a small value of L_{out} , the profile of the outflow does not satisfy the sufficient condition of the linear stability, and the long waves originated from the eastern boundary can propagate eastward without matching with the western boundary condition. Thus, these small values of L_{out} were not examined in the present study. The value of L_{out} used in experiments N5 and N10U8 was close to this limit. The value of j_{out} is offset by the stretching term by a constant amount independent of L_{out} .

The meridional dimension of the basin Y was also changed, in order to examine more examples of j_{out} . The value of j_{out} increases with Y because of the planetary beta effect, when L_{out} is large and satisfies $Y \leq L_{\text{out}}$ (e.g., experiments Sinf, Ninf, and Linf). The amplitude of the inflow and outflow u_0 was doubled in experiments N10U8, NinfU8, L15U8, and LinfU8. The total transport of the inflow and outflow was 15 and 30 Sv ($1 \text{ Sv} \equiv 10^6 \text{ m}^3 \text{ s}^{-1}$) for $u_0 = 0.4$ and 0.8 m s^{-1} , respectively. These values are roughly comparable to the net eastward transport of the Kuroshio (Imawaki et al. 2001).

The velocity and density were nudged to the boundary values near the western and eastern boundaries, at which a radiation condition was imposed. The southern and northern boundaries were solid and a sponge layer was imposed along the boundaries to suppress the reflection of waves. The nudging and sponge layer were the same as in Mizuta (2009). Bottom friction with the damping time scale of 1000 days was included as dissipation. In ROMS, the third-order upstream horizontal advection and the fourth-order centered horizontal advection were used for the momentum and tracer, respectively. Hence, the model included numerical viscosity. Horizontal grid spacings were 10 km, and vertical grid spacings were 11 m near the surface and the bottom and increased to 335 m at middle depths.

Model equations were integrated for 8000 days for each experiment in Table 1, starting from a zonal jet that has the same profile as that imposed at the western boundary and an initial perturbation that consists of a Gaussian eddy of 30-km radius. After the spinup of 4000 days, during which the initial trend of the total kinetic energy attenuates, the motions obtained for the last 4000 days were analyzed. The sensitivity of the model results to the distance to the eastern boundary and vertical grid spacings was also investigated by increasing the

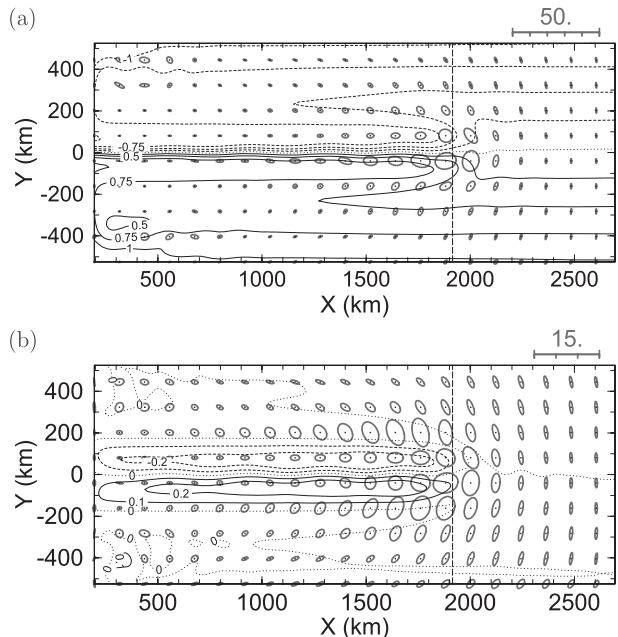


FIG. 1. Mean Bernoulli function $\bar{\Pi}$ and variance ellipses that represent (u', v') on (a) the $26.3\text{-}\sigma_\theta$ surface and (b) the $27.8\text{-}\sigma_\theta$ surface. The areas near the boundaries are omitted. The vertical lines correspond to $x = x_c$. See the text for the definition of x_c .

domain width and the grid numbers in the vertical direction. The experimental results were found to vary little with these changes.

3. Effect of the Rossby waves on the mean flow

In this section, we first examine the basic structure of the mean flow and variabilities in a typical example. Then, we examine the structure of the eddy potential vorticity flux, the character of the radiation of the Rossby waves, and the effect of the Rossby waves on the mean flow.

The mean flow and variabilities obtained in experiment Ninf are examined as a typical example (Fig. 1). In the following analysis, the flows on the 26.3- and $27.8\text{-}\sigma_\theta$ isopycnal surfaces, which are located at depths approximately 400 and 3300 m, are adopted as being representative of the surface and deep flows, respectively. These depths correspond to the upper part of the pycnocline and the part below the pycnocline. The velocity (u, v) ; isopycnal depth z ; and Bernoulli function Π , which corresponds to the quasigeostrophic streamfunction in isopycnal coordinates, are interpolated onto these isopycnals in 4-day intervals, and the potential vorticity q on the isopycnals is calculated from the interpolated variables. Then, the time averages, which are denoted by overbars, and the deviations from the time average, which are denoted by primes, are obtained for these variables.

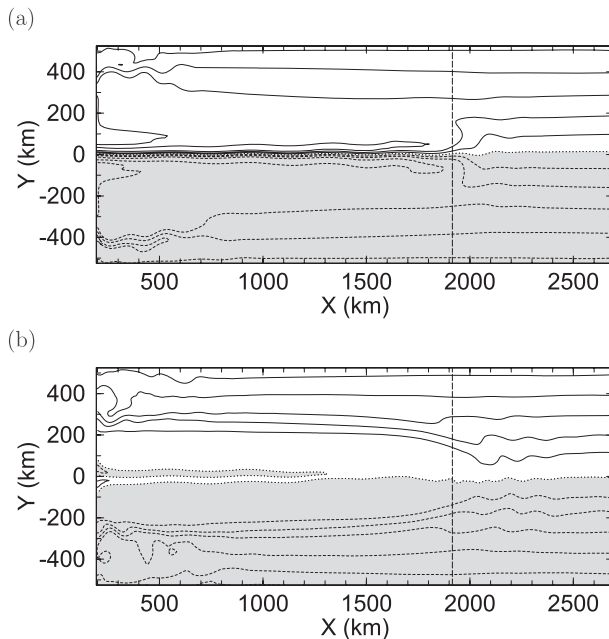


FIG. 2. Mean potential vorticity \bar{q} on (a) the 26.3- σ_θ surface and (b) the 27.8- σ_θ surface. The shaded regions indicate the region of negative \bar{q} . The vertical lines correspond to $x = x_c$.

Driven by the inflow from the western boundary, an eastward jet is formed at $y \sim 0$ in the mean field in the western region of the model domain (Fig. 1a). The jet extends from $(26.3\text{--}27.8)\sigma_\theta$ (Figs. 1a,b). The jet is flanked by westward recirculations especially on the 27.8- σ_θ surface. There is a front of the mean potential vorticity along the jet axis on the 26.3- σ_θ surface (Fig. 2a), whereas the mean potential vorticity in this region is nearly homogeneous on the 27.8- σ_θ surface (Fig. 2b), as indicated by the results of the numerical experiment of wind-driven circulation (Holland and Rhines 1980). The meridional gradient of the mean potential vorticity is negative on both sides of the jet and along the jet axis on the 26.3- and 27.8- σ_θ surfaces, respectively, satisfying the necessary condition of both barotropic and baroclinic instability.

Driven by the outflow from the eastern boundary, a broad and almost parallel flow, which is in the eastward direction, is formed on the 26.3- σ_θ surface in the eastern region of the model domain (Fig. 1a). Because the mean potential vorticity is approximately constant in the zonal direction and takes a value close to that on the eastern boundary due to the planetary beta effect (Fig. 2a), this region will hereafter be referred to as the interior region. In the region between the western and interior regions, the jet is broadened at $x \sim 2000$ km and mostly continues eastward on the 26.3- σ_θ surface, whereas flows return to the western region on the 27.8- σ_θ surface. This region will be referred to as the transient region. As an indicator of

the center of the transient region, the dashed lines in Figs. 1 and 2 denote $x = x_c$, which is defined as $x_c = (x_{c1} + x_{c2})/2$, with x_{c1} and x_{c2} being the maxima of the barotropic meridional velocity in the southern and northern halves of the domain, respectively. The difference in the potential vorticity between the inflow and outflow must be eliminated somewhere in the western and transient regions before flows enter the interior region, especially on the 26.3- σ_θ surface, on which the transport of the inflow and outflow is large. The three regions similar to the present study have been identified by Waterman and Jayne (2011) based on the character of baroclinic and barotropic instability and the eddy potential vorticity flux.

The meridional profile of the mean zonal velocity on the 26.3-, 27.1-, 27.7-, and 27.8- σ_θ surfaces are compared in Fig. 3a, where these isopycnal surfaces are located at depths of approximately 400, 1100, 2200, and 3300 m, respectively. The maxima of the recirculations are located at $y \sim \pm 150$ km, with the maximum speed being ~ 4 cm s^{-1} on these isopycnal surfaces. The maximum speed of the jet and the magnitude of the front of the mean potential vorticity at the jet axis decrease monotonically with depth, and the front is absent from the 27.8- σ_θ surface (Figs. 3a,b). The meridional gradient of the mean potential vorticity in the southern and northern recirculations is smaller than that outside the recirculation, where the planetary potential vorticity is dominant, on these isopycnal surfaces (Fig. 3b). Thus, the present study adopts the 26.3- and 27.8- σ_θ surfaces as being two typical isopycnals.

The variance of the velocity is large on the 26.3- σ_θ surface along the jet axis (Fig. 1). The variance increases in the eastward direction and reaches a maximum in the transient region on both the 26.3- and 27.8- σ_θ surfaces (Fig. 1). A large variance extends over a broader area on the 27.8- σ_θ surface than on the 26.3- σ_θ surface. Because the major axes of the variance ellipses are oriented in the northwest-southeast direction in the northern part and are oriented in the southwest-northeast direction in the southern part, it is suggested that energy is radiated from the jet by the Rossby waves. Mizuta (2009) showed that the variabilities of velocity are dominated by the barotropic Rossby waves, except for those near the jet and recirculation.

The eddy potential vorticity flux $\overline{\mathbf{u}'q'}$ on the 26.3- σ_θ surface converges and diverges in the northern and southern parts of $x \sim 2000$ km, which corresponds to the transient region (Fig. 4a). This dipole structure of the convergence of $\overline{\mathbf{u}'q'}$ tends to accelerate cyclonic and anticyclonic circulations in the northern and southern parts, respectively. The convergence of $\overline{\mathbf{u}'q'}$ in the western region has the opposite sign from that in the transient region in similar latitudes. Thus, the eddy potential vorticity

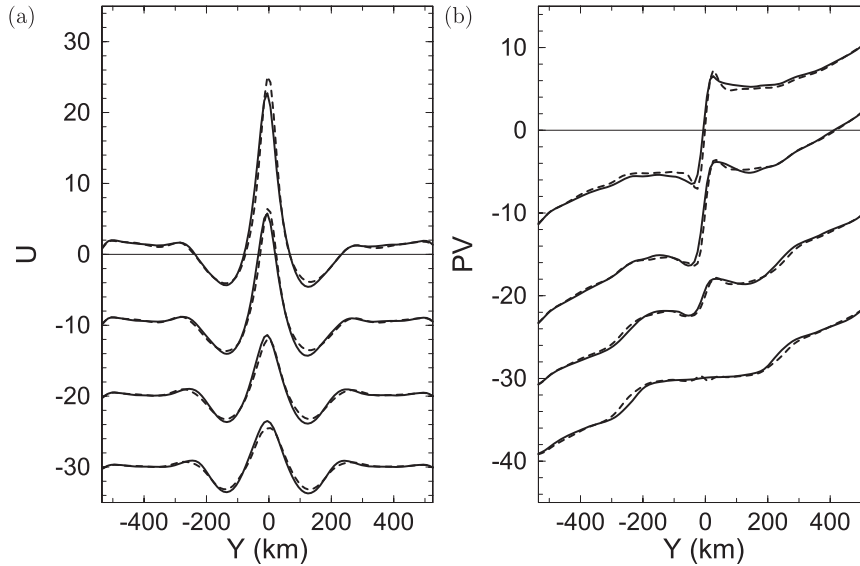


FIG. 3. Meridional distribution of (a) the mean zonal velocity \bar{u} (cm s⁻¹) and (b) the mean potential vorticity \bar{q} (10⁻⁶ s⁻²) in experiment Ninf. The top, upper middle, lower middle, and bottom lines indicate the distribution on the 26.3-, 27.1-, 27.7-, and 27.8- σ_θ surfaces, respectively. The solid and dashed lines denote the distributions along $x = 1500$ and 1000 km, respectively.

flux tends to decelerate cyclonic and anticyclonic circulations on cyclonic and anticyclonic sides of the jet, respectively, suggesting barotropic or mixed instability. The relative vorticity flux dominates in the potential vorticity flux on this isopycnal surface (Figs. 4b,c). Decreasing with depth, the relative vorticity flux near the jet and recirculation is comparable to the potential thickness flux on the 27.8- σ_θ surface, and the dipole structure is not

dominant on this surface (not shown). The convergence of the eddy potential vorticity flux $\overline{\mathbf{u}'q'}$ almost cancel with that of the mean potential vorticity flux $\overline{\mathbf{u}\bar{q}}$ in most of the model domain, except for a narrow region near the jet axis, indicating that the region of significant dissipation is limited (Fig. 4d).

The dipole structure of the convergence of $\overline{\mathbf{u}'q'}$ on the 26.3- σ_θ surface is qualitatively similar to that in an

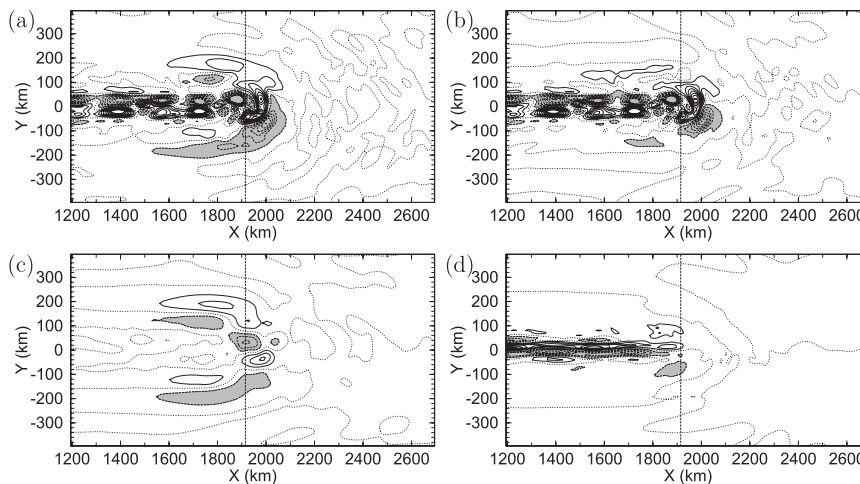


FIG. 4. Convergence of (a) the eddy potential vorticity flux $-\nabla \cdot \overline{\mathbf{u}'q'}$, (b) the eddy relative vorticity flux $-\nabla \cdot \overline{\mathbf{u}'\zeta'}$, (c) the eddy potential thickness flux $-f_0 \nabla \cdot \overline{\mathbf{u}'(b'/N^2)_2}$, and (d) the sum of the mean and eddy potential vorticity flux $-\nabla \cdot (\overline{\mathbf{u}\bar{q}} + \overline{\mathbf{u}'q'})$ on the 26.3- σ_θ surface in experiment Ninf. The contour interval is $ci = 5 \times 10^{-14}$ (s⁻²) with the shaded regions indicating the regions in which the convergence is $< -ci$. The vertical dashed lines in each panel correspond to $x = x_c$.

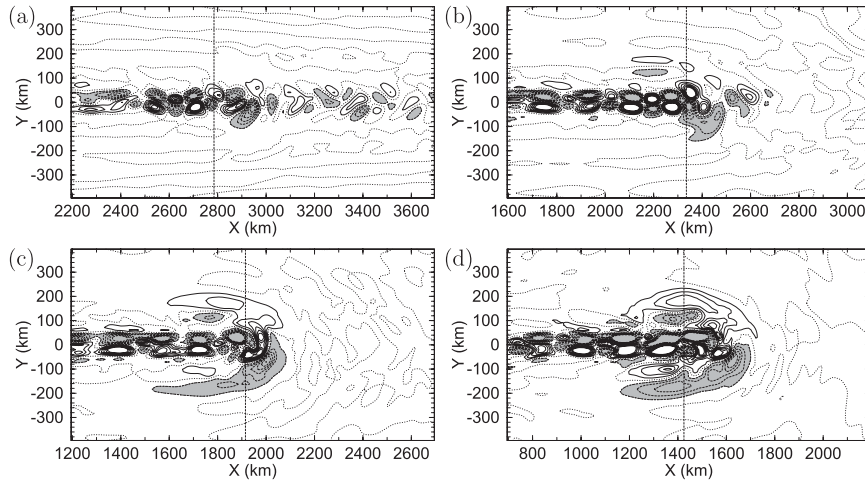


FIG. 5. Convergence of the eddy potential vorticity flux $-\nabla \cdot \overline{\mathbf{u}'q'}$, on the $26.3\text{-}\sigma_\theta$ surface in experiments (a) N5, (b) N10, (c) Ninf, and (d) Linf. The contour interval is $ci = 5 \times 10^{-14} \text{ (s}^{-2}\text{)}$, with the shaded regions indicating the regions in which $-\nabla \cdot \overline{\mathbf{u}'q'} < -ci$. The vertical dashed lines in each panel correspond to $x = x_c$.

idealized experiment conducted by Haidvogel and Rhines (1983), who examined the Rossby waves excited by a localized forcing in a circular region. In their experiment, $\overline{\mathbf{u}'q'}$ is northward in the region where the forcing to the wave is applied, and $\overline{\mathbf{u}'q'}$ converges and diverges in the northern and southern parts of the forcing region, respectively. In the following, we further examine the relationship between the dipole structure and the wave radiation, by comparing results from different experiments.

The convergences of the eddy potential vorticity flux in four experiments are compared in Fig. 5 as typical examples. The mean potential vorticity of the outflow j_{out} scaled with $u_0 L_{\text{in}}^{-1}$ is 0.45, 0.56, 0.69, and 0.95, in Figs. 5a–d,

respectively, and increases in this order (Table 1). The dipole structure of the potential vorticity flux convergence is apparent in the experiments other than experiment N5 (Fig. 5a). The dashed lines in each figures in Figs. 5 and 6 denote the center of the transient region, $x = x_c$. In these experiments, the dipole is located in the transient region where the jet is broadened and matched to the interior flow. The intensity of the dipole increases systematically with the potential vorticity of the outflow j_{out} (Fig. 5). The value of x_c varies from $x_c \sim 2800$ km in experiment N5 to $x_c \sim 1400$ km in experiment Linf as the zonal width of the western region varies between these experiments. The change of the zonal width may be related to that of the e -folding scale in time and/or space of the instability of

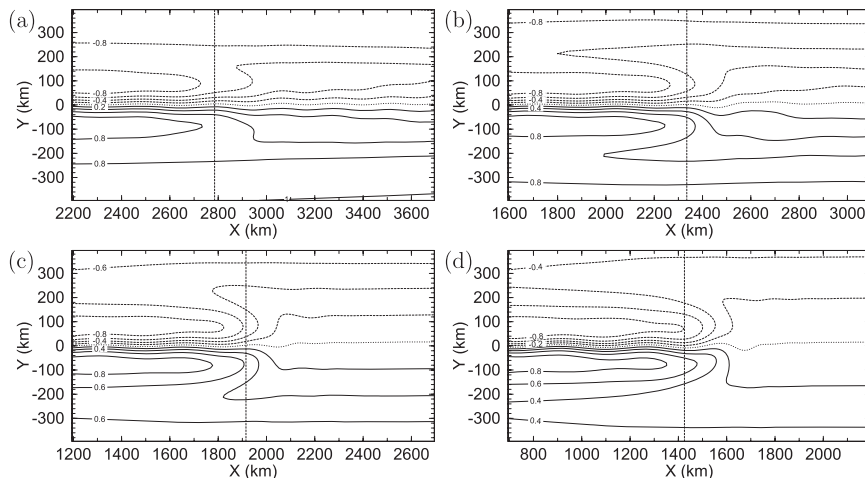


FIG. 6. As in Fig. 5, but for the mean Bernoulli function. The contour interval is $0.2 \text{ m}^2 \text{ s}^{-2}$.

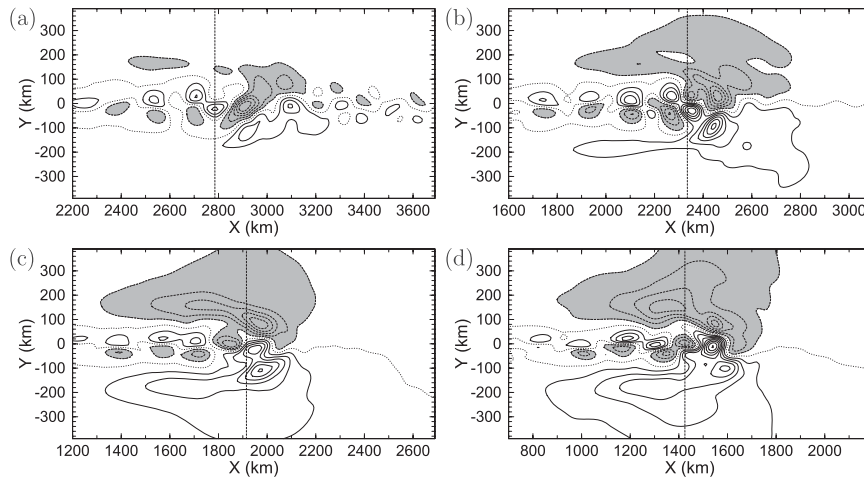


FIG. 7. As in Fig. 6, but for the vertically averaged Reynolds stress. The contour interval is $ci = 0.4 \text{ (cm}^2 \text{ s}^{-2}\text{)}$, with the shaded regions indicating the regions in which the integrated Reynolds stress is $< -ci$.

the jet (Jayne and Hogg 1999). However, determining the precise reason for this change is beyond the scope of the present study.

The character of the Rossby wave radiation is examined, by using the distribution of the Reynolds stress $\overline{u'v'}$ that is averaged in the vertical direction (Fig. 7). The Reynolds stress $\overline{u'v'}$ is nonzero in regions where the Rossby waves propagate over a long distance in the meridional direction without being dissipated or forced. This is not the case for the convergence of the eddy potential vorticity flux due to the nonacceleration theorem (Fig. 5). The Reynolds stress $\overline{u'v'}$ in experiment Ninf is negative (positive) in the northern (southern) part of the basin, corresponding to the orientation of the major axis of variance ellipses shown in Fig. 1 (Fig. 7c). A maximum and a minimum of $\overline{u'v'}$ are located in the transient region. The Reynolds stress $\overline{u'v'}$ integrated in the zonal and vertical direction in experiment Ninf is examined in Fig. 8. The integrated Reynolds stress is approximately constant in the meridional direction outside the jet and recirculation, $|y| > 250 \text{ km}$, indicating that the Rossby waves propagate without the forcing and dissipation there (Fig. 8). Thus, the present study adopts the amplitude of $\overline{u'v'}$ outside the recirculation as a measure of the intensity of the Rossby waves radiated from the jet and recirculation.

The same (qualitatively) feature of the horizontal distribution of the Reynolds stress is observed in other experiments in Fig. 7. As in Fig. 5, Figs. 7a–d are displayed in the increasing order of the mean potential vorticity of the outflow j_{out} . The Reynolds stress indicates that the Rossby wave radiation is intensified with j_{out} . Thus, the intensity of the Rossby wave and that of the dipole of

the convergence of the eddy potential vorticity flux are correlated with each other. According to a precise analysis in which motions are divided into frequency bands, the dipole structure in Fig. 5 is due to low-frequency motions, which are dominated by the Rossby waves (Mizuta 2009). Similarly, the potential vorticity flux convergence along the jet axis in the western region is due to high-frequency motions concentrated near the jet. Therefore, the dipole structure in Fig. 5 is due to the wave radiation.

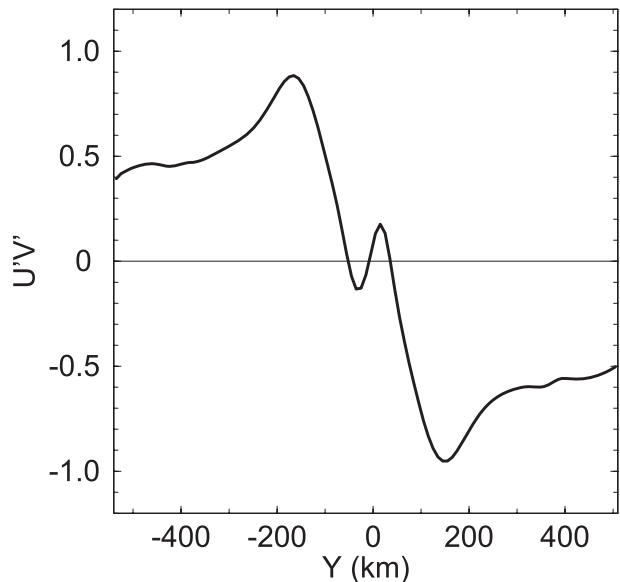


FIG. 8. Meridional distribution of the Reynolds stress $\overline{u'v'}$ integrated in the zonal and vertical directions ($10^2 \text{ m}^4 \text{ s}^{-2}$) in experiment Ninf.

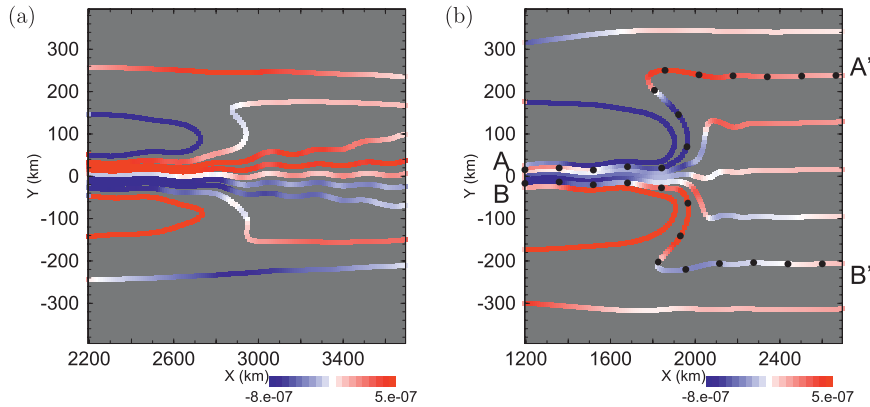


FIG. 9. Distribution of $\delta\bar{q}$ along contours of $\bar{\Pi}$ in experiments (a) N5 and (b) Ninf. Colors indicate the value of $\delta\bar{q}$. The contour interval is $0.2 \text{ m}^2 \text{ s}^{-2}$. The dotted lines A–A' and B–B' in (b) indicate typical contours that pass through the northern and southern parts of the transient region, respectively.

In the following, we further examine how the wave radiation affects the mean flow. To examine the relationship between $\overline{\mathbf{u}'q'}$ and the change of \bar{q} along mean streamlines, \bar{q} is divided into two components,

$$\bar{q} = Q(\bar{\Pi}) + \delta\bar{q}, \quad (7)$$

where $Q(\bar{\Pi})$ denotes a representative value of the mean potential vorticity along a prescribed contour of $\bar{\Pi}$ and $\delta\bar{q}$ denotes the deviation of \bar{q} from this mean potential vorticity. Then, only the second term, the magnitude of which is expressed by colors in Fig. 9, contributes to advection of \bar{q} to the first approximation. The form of $Q(\bar{\Pi})$ was determined by means of a polynomial fitting of \bar{q} in the interior region by $\bar{\Pi}$ for each experiment and differs between Figs. 9a,b.

We first examine the change in $\delta\bar{q}$ along contour A–A', which passes through the northern part of the transient region in experiment Ninf, starting from point A (Fig. 9b). The value of $\delta\bar{q}$ is high at point A, which is located on the cyclonic side of the jet. Then $\delta\bar{q}$ decreases eastward along the contour in the region $1200 \lesssim x \lesssim 1900$ km near the jet axis. This part of the contour is located in the area, in which $\overline{\mathbf{u}'q'}$ diverges, presumably because of instability (Fig. 5c). The value of $\delta\bar{q}$ is negative at $(x, y) \sim (1900, 20)$ km and increases along the contour in the region $50 \lesssim y \lesssim 250$ km as the jet broadens. This part of the contour is located in the northern part of the dipole of the convergence of $\overline{\mathbf{u}'q'}$ associated with the Rossby wave radiation (Fig. 5c). The value of $\delta\bar{q}$ along contour B–B' that passes through the southern part of the transient region in experiment Ninf, changes in the opposite manner from contour A–A'. That is, $\delta\bar{q}$ increases because of the instability of the jet in the western and transient regions and decreases because of the Rossby wave radiation as the jet

broadens in the transient region. Note that \bar{q} along contour A–A' is larger than that along contour B–B' if the contribution from $Q(\bar{\Pi})$ is included. Thus, instability excessively reduces the difference in \bar{q} between the two contours as compared with that of the interior flow, and the radiation of the Rossby waves compensates for the reduced difference. When the width of outflow is narrower and hence the mean potential vorticity of the outflow j_{out} is smaller, the change of $\delta\bar{q}$ associated with the broadening of the jet is not clear, corresponding to the weak radiation of the Rossby waves (Fig. 9a).

The correlation between the potential vorticity of the outflow j_{out} , and the intensity of the Rossby waves is examined in Fig. 10 for all of the experiments listed in Table 1. Here, the Reynolds stress $\overline{u'v'}$ outside the jet and recirculation is adopted as the intensity of the Rossby waves. Because $l_\beta = \sqrt{u_0/\beta}$ is a typical meridional scale of the recirculation (Mizuta 2009), the difference in the Reynolds stress, which is integrated on $y = \pm 2l_\beta$ in the zonal and vertical directions, is adopted in Fig. 10. The value of $2l_\beta$ corresponds to 280 and 400 km for $u_0 = 0.4$ and 0.8 m s^{-1} , respectively, and the integrated Reynolds stress is approximately constant in the meridional direction near $y = \pm 2l_\beta$ (Fig. 8).

The intensity of the Rossby wave increases systematically with the potential vorticity of the outflow, except for one experiment for $u_0 = 0.8 \text{ m s}^{-1}$ (Fig. 10). Therefore, the change in the mean potential vorticity associated with the broadening of the jet in the meridional direction is compensated for by the potential vorticity flux by the Rossby wave radiation. Note that experiments with various combinations of the outflow width L_{out} and domain size Y are aligned near a single curve on the $j_{\text{out}}-\overline{u'v'}$ plane, especially for $u_0 = 0.4 \text{ m s}^{-1}$. The integrated Reynolds stress is partitioned into the contribution from

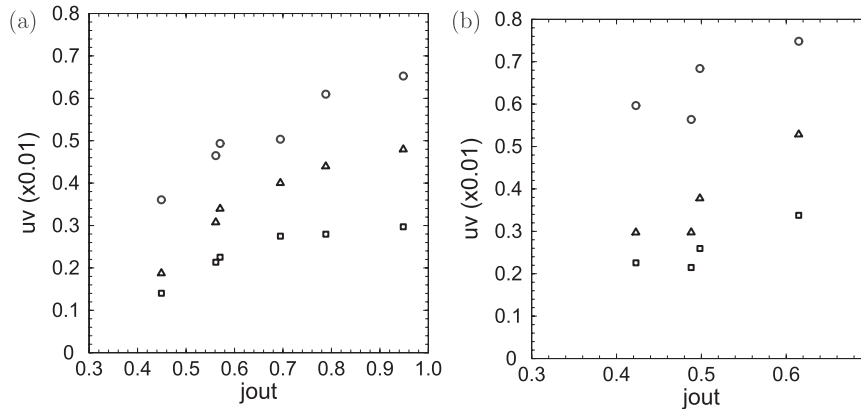


FIG. 10. Scatterplots of j_{out} vs the Reynolds stress $\overline{u'v'}$ integrated in the zonal and vertical directions in all experiments for $u_0 =$ (a) 0.4 and (b) 0.8 $m s^{-1}$. The circles, triangles, and squares indicate the Reynolds stress integrated in $0 < x$, $0 < x < x_c + \lambda$, and $0 < x < x_c$, respectively. The values of j_{out} and integrated Reynolds stress are normalized with $u_0 L_{in}^{-1}$ and $u_0^2 l_{\beta} H_0$, respectively.

the intervals $0 < x$ (circle), $0 < x < x_c + \lambda_0$ (triangle), and $0 < x < x_c$ (square), where $\lambda_0 = 400$ km is a typical value of the wavelength of the Rossby waves. The contribution from $x_c + \lambda_0 < x$ (circle minus triangle) is about 0.1–0.2 for $u_0 = 0.4$ $m s^{-1}$ and 0.2–0.3 for $u_0 = 0.8$ $m s^{-1}$, and it does not increase significantly with j_{out} for $u_0 = 0.4$ $m s^{-1}$ and decreases with increasing j_{out} for $u_0 = 0.8$ $m s^{-1}$, suggesting that the increase of the short Rossby waves is rather small (Fig. 10). Thus, we focus on the Rossby waves radiated into the western and transient regions in the next section.

Before proceeding to the next section, some remarks are added to the effect of the inflow width on the mean potential vorticity. The minimum of $\delta\bar{q}$ along contour A–A' and the maximum of $\delta\bar{q}$ along contour B–B' in experiment Ninf (Fig. 9b) are listed in Table 2. The minimum $\delta\bar{q}_{min}$ and maximum $\delta\bar{q}_{max}$ are negative and positive, respectively, corresponding to the effect of instability. For comparison, the width of inflow L_{in} is increased by 20% with the total transport of the inflow and the outflow condition unchanged in experiment NinfB (Table 2). Both $|\delta\bar{q}_{min}|$ and $|\delta\bar{q}_{max}|$ decrease with increasing L_{in} , corresponding to the weakening of the perturbation of the jet by instability (the maximum of the rms of the potential vorticity on the $26.3\text{-}\sigma_{\theta}$ surface is 3.7 and 2.3 in experiments Ninf and NinfB, respectively). This feature of $\delta\bar{q}$ is may not be surprising, if we consider

a limit, in which L_{in} is increased to the same value as L_{out} . In this limit, streamlines are zonal and $\delta\bar{q}$ vanishes. However, quantitative analysis of the change of $\delta\bar{q}$ by intrinsic dynamics of the jet is beyond the scope of the present study. The Reynolds stress integrated in the zonal and vertical direction indicates again that the radiation of the Rossby waves decreases with $|\delta\bar{q}_{min}|$ and $|\delta\bar{q}_{max}|$ (Table 2). Qualitatively same results are obtained in experiments with $u_0 = 0.8$ $m s^{-1}$ (not shown).

4. Radiation process of the Rossby waves

In the previous section, the intensity of the Rossby waves is shown to increase with the mean potential vorticity of the outflow in order to compensate for difference in the potential vorticity between the inflow and outflow. In this section, the source of the Rossby waves and the process that adjusts the wave intensity to a value that is appropriate to the difference between the inflow and outflow are examined. The zonal phase speed of the Rossby waves tends to be close to the maximum speed of the recirculation (Mizuta 2009). Because advection by the mean flow is expected to be dominant in the variabilities of the potential vorticity in the recirculation, in which the mean potential vorticity is nearly homogeneous, it is most probable that the waves are related to the variabilities in

TABLE 2. The minimum and maximum of $\delta\bar{q}$ along typical mean streamlines that pass through the northern and southern parts of the transient region, respectively. The fifth, sixth, and last columns represent the minimum of $\delta\bar{q}$ along a streamline $\bar{\Pi} = \bar{\Pi}_N$, the maximum of $\delta\bar{q}$ along a streamline $\bar{\Pi} = \bar{\Pi}_S$; and the Reynolds stress $\overline{u'v'}$ integrated in the zonal and vertical direction at $y = 2l_{\beta}$, respectively. The values in parentheses in the fifth and sixth columns denote $\bar{\Pi}_N$ and $\bar{\Pi}_S$, respectively.

	u_0 ($m s^{-1}$)	L_{in} (km)	L_{out} (km)	$\delta\bar{q}_{min}(\bar{\Pi}_N)$ ($10^{-6} s^{-1}$)	$\delta\bar{q}_{max}(\bar{\Pi}_S)$ ($10^{-6} s^{-1}$)	Integrated $\overline{u'v'}$ ($10^6 m^4 s^{-2}$)
Ninf	0.4	30	∞	-1.22 (-0.4, A–A')	0.85 (0.4, B–B')	0.46
NinfB	0.33	36	∞	-0.86 (-0.4)	0.72 (0.4)	0.27

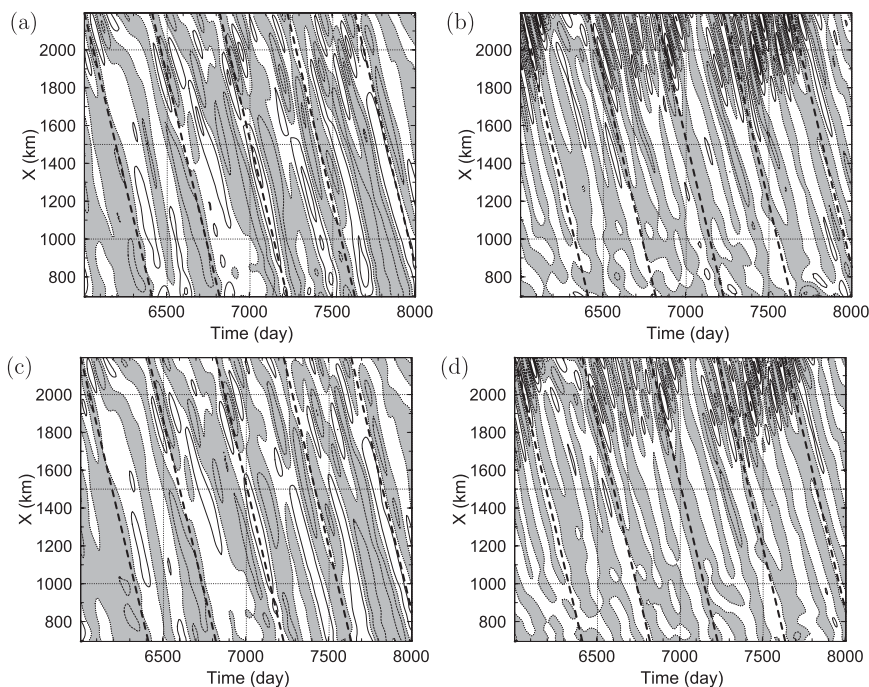


FIG. 11. Hovmoeller diagrams of (a) u' on the $26.3\text{-}\sigma_\theta$ surface, (b) v' on the $26.3\text{-}\sigma_\theta$ surface, (c) u' on the $27.8\text{-}\sigma_\theta$ surface, and (d) v' on the $27.8\text{-}\sigma_\theta$ surface along $y = 400$ km. The thick dashed lines in each panel correspond to the westward-propagating speed of $c_x = 4.3$ cm s $^{-1}$. The contour interval is 0.8 cm s $^{-1}$, with the shaded regions indicating the region of negative u' or v' .

the recirculation. This property of the Rossby waves is apparent in the Hovmoeller diagram of the velocity at a latitude to the north of the northern recirculation (Fig. 11). The variabilities of the velocity are approximately barotropic and propagate at an almost constant speed during most of the period in $x < 2200$ km, even though the barotropic Rossby waves are dispersive. The waves are not monochromatic, because low-frequency motions are more dominant in the zonal velocity u' than in the meridional velocity v' . Thus, the variabilities in Fig. 11 are the sum of the waves that satisfy $c_x = -\beta/(k^2 + l^2) = \text{const}$, where c_x is the zonal phase speed and k (l) is the zonal (meridional) wavenumber. This constraint implies that the ratio $|k|/|l|$ increases with frequency, $\omega = kc_x$, and is consistent with the difference in frequency between u' and v' in Fig. 11. The dominant zonal phase speed, $c_x \sim 4.3$ cm s $^{-1}$, is close to the maximum westward speed of the recirculation U_m (Fig. 3a). Mizuta (2009) hypothesized that eddies advected westward within the recirculation, in which the mean potential vorticity is nearly homogeneous, are the source of the Rossby waves. We first validate this hypothesis in section 4a.

a. Source of the Rossby waves

The variabilities of velocity are large near the jet and recirculation on shallow isopycnals (Fig. 1). The rms of

eddy potential vorticity on the $26.3\text{-}\sigma_\theta$ surface attains maxima in the meridional direction along the jet axis, $y \sim 0$, and the recirculation, $y \sim \pm 150$ km, in experiment Ninf in which the Rossby waves are apparent (Fig. 12c). The evolution of eddies along the jet, in the transient region, along the recirculation, and at a longitude in the western region is examined in Figs. 13a–d, respectively, by using Hovmoeller diagrams of the eddy potential vorticity. Eddies in the jet move eastward in the western and transient regions, $x \lesssim 2000$ km (Fig. 13a). Although standing waves are suggested by patches of the eddy potential vorticity with a zonal scale of ~ 100 km, the westward-propagating motions appear to be rather minor.

The above-mentioned area, which is characterized by intense eddies, ends in the transient region, in which eddies move northward and southward from the jet axis, $y \sim 0$ km, to the recirculation, $y \sim \pm 150$ km (Fig. 13b). Potential vorticity anomalies are shed northward from the jet axis at approximately 6100, 6600, 7100, and 7300 days. Contours of the potential vorticity near the jet are distorted from horizontal lines by $O(10^2)$ km in the meridional direction around these days. Note that the contours of the potential vorticity to the north of the recirculation, $y > 250$ km, appear to be disturbed after this shedding of eddies. Dominated by the planetary potential vorticity, the meridional gradient of the potential vorticity is always

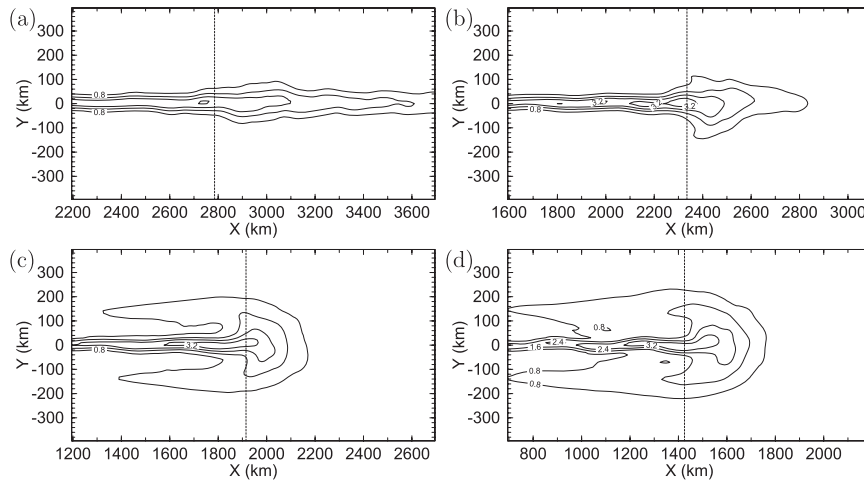


FIG. 12. As in Fig. 7, but for the rms of the potential vorticity $(q'^2)^{1/2}$ on the $26.3\text{-}\sigma_\theta$ surface. The contour interval is 0.8 s^{-1} .

positive in $|y| > 250\text{ km}$. This is consistent with the fact that the variabilities in these areas are dominated by the linear Rossby waves. The distortion of contours of the potential vorticity from horizontal lines is an order of magnitude smaller in $|y| > 250\text{ km}$ than that in the recirculation. In contrast to the variabilities in $|y| > 250\text{ km}$,

there are minima and maxima of the potential vorticity in the meridional direction in the northern and southern recirculations, where the mean potential vorticity is approximately homogeneous, except for $y \sim 0$ (Fig. 3b). Some contours of the potential vorticity are closed around these minima and maxima. These closed contours and the

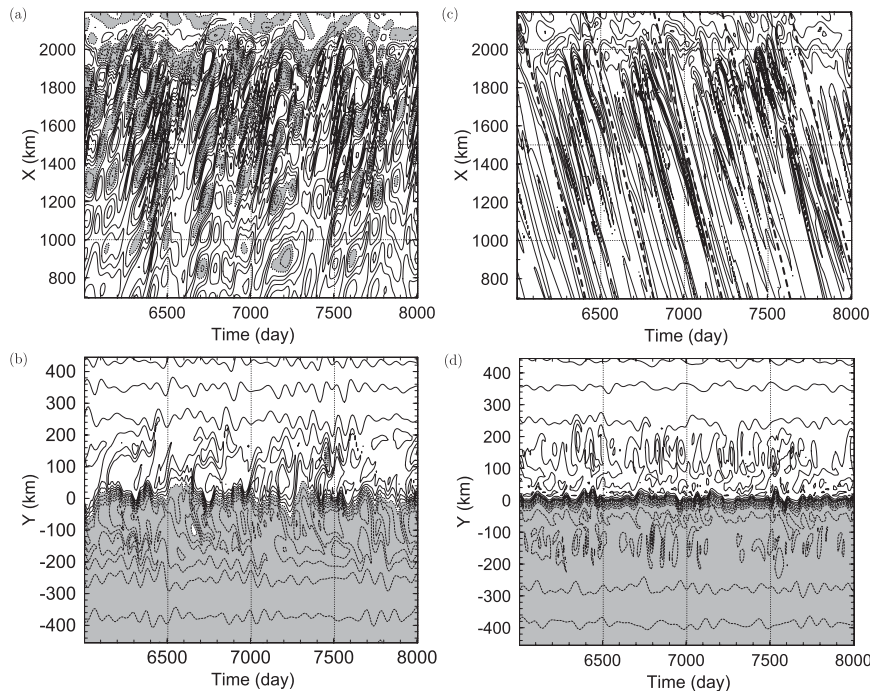


FIG. 13. Hovmoeller diagrams of q' on the $26.3\text{-}\sigma_\theta$ surface in experiment Ninf along (a) $y = 0\text{ km}$, (b) $x = 1950\text{ km}$, (c) $y = 150\text{ km}$, and (d) $x = 1500\text{ km}$. The location $x = 1950\text{ km}$ adopted in (b) corresponds to the maximum of meridional velocity in the northern half of the domain ($x = x_{c2}$). The thick dashed lines in (c) correspond to the westward-propagating speed of $c_x = 4.3\text{ cm s}^{-1}$. The contour interval is 1.5 s^{-1} in (a),(b),(d) and 0.75 s^{-1} in (c).

large distortion of contours from horizontal lines indicate nonlinearity of the variabilities inside the recirculation. Eddies characterized by closed contours of the potential vorticity are in contrast to the linear waves outside the recirculation due to this nonlinearity.

Eddies that have entered the recirculation move westward at an almost constant speed (Fig. 13c). This speed is close to 4.3 cm s^{-1} and coincides with that of the Rossby waves radiated to the north of the recirculation (Fig. 11). Shedding of eddies from the jet is absent from the western region at $x = 1500 \text{ km}$ (Fig. 13d). The variabilities of the potential vorticity at this longitude again consist of eddies characterized with closed contours of potential vorticity within the recirculation and the linear waves to the north and south of the recirculation.

The behavior of the eddy potential vorticity shown in Fig. 13 supports the hypothesis that the variabilities by eddies in the recirculation are the source of the Rossby waves. Examples of this type of the source of the waves can be demonstrated in an initial value problem of eddies posed in a piecewise basic flow in a zonally periodic channel (Fig. 14). The essential feature of the problem is described in the following for a two-layer problem. A two-layer model is employed to the lowest order of approximation in the present study in order to represent the flows on the 26.3 and $27.8 \sigma_\theta$ surfaces in numerical experiments (Fig. 3). An analytic solution in a barotropic problem is shown in detail in the appendix of Mizuta (2009).

We consider the following two-layer quasigeostrophic equation:

$$\left(\frac{\partial}{\partial t} + U_n \frac{\partial}{\partial x}\right) [\nabla^2 \psi_n + (-1)^n F_n (\psi_1 - \psi_2)] + Q_{n,y} \psi_{n,x} = 0 \quad (n = 1, 2), \quad (8)$$

where t is the time; U_1 and U_2 are the basic zonal flows in the upper and lower layers, respectively, ψ_1 and ψ_2 are the perturbation streamfunctions; ∇^2 is the Laplacian in the horizontal direction; and $F_n = f_0^2 / (g' H_n)$, with g' and H_n representing the reduced gravity and layer thickness, respectively. The basic flow U_n , which is absent in the region $|y| > D$, is defined in appendix A, and the basic potential vorticity Q_n determined from this U_n satisfies

$$Q_{n,y} = \begin{cases} 0 & \text{at } 0 < |y| < D \\ \beta & \text{at } |y| > D \end{cases}, \quad (9)$$

with

$$[Q_1]_0 = 2\Delta Q, \quad [Q_2]_0 = 0, \quad (10)$$

indicating that Q_n is homogeneous in $0 < |y| < D$, which corresponds to the recirculation. The basic flow in the

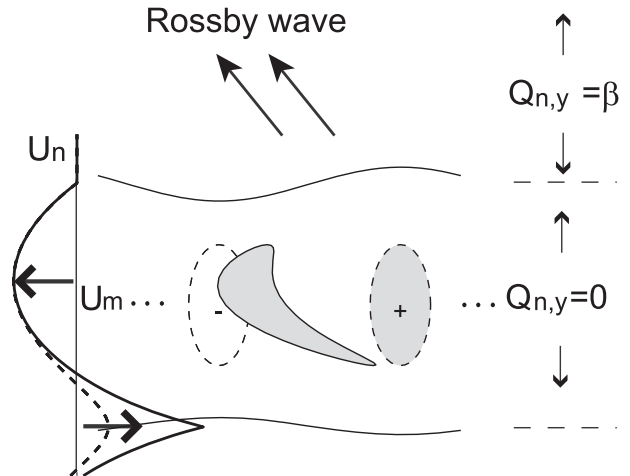


FIG. 14. Schematic diagram of an analytic model with a piecewise basic flow. The thick solid and thick dashed lines indicate the meridional profile of the basic flow in the upper and lower layers, respectively. The letter U_m indicates the minimum of the basic flow in the upper layer. The solid lines indicate the material surfaces, which are initially located at $y = 0, D$. From (9) and (10), Q_1 and $Q_{n,y}$ ($n = 1, 2$) are discontinuous at $y = 0$ and D , respectively. The dashed ellipses indicate contours of the perturbation potential vorticity prescribed as the initial condition. The shaded regions correspond to the same fluid particles at two different times.

upper layer is eastward near $y = 0$ and westward to the north and south of $y = 0$ (Fig. 14), when ΔQ satisfies (A5). Thus, the qualitative features of the mean flow and the mean potential vorticity in the numerical experiments are roughly captured.

The perturbation streamfunctions are assumed to be periodic in the zonal direction. That is,

$$\psi_n = \phi_n e^{ikx}. \quad (11)$$

Because the last term on the lhs of (8) vanishes in the recirculation, $0 < |y| < D$, the value of the perturbation potential vorticity is nonzero there only if a nonzero value is initially prescribed (Pedlosky 1964). The normal modes of (8) do not change the potential vorticity in $0 < |y| < D$. The large variabilities of the jet shown in Fig. 13b are absent from the linearized equation, (8). Thus, a perturbation potential vorticity $q_0(y)e^{ikx}$ that corresponds to closed contours of the potential vorticity is initially prescribed in the upper layer of the northern recirculation, $0 < y < D$,

$$q_n = \phi_{n,yy} - k^2 \phi_n + (-1)^n F_n (\phi_1 - \phi_2) = q_0 \delta_{n1} \quad \text{at } t = 0. \quad (12)$$

Using the method of Laplace transformation in time, we have

$$\tilde{\phi}_n = \int_0^D -\frac{iG_n(y; y', p)q_0(y')}{kU_1 - ip} dy', \quad (13)$$

where

$$\tilde{\phi}_n = \int_0^\infty \phi e^{-pt} dt. \quad (14)$$

Here, $G_n(y; y', p)$ is the Green's function and satisfies

$$G_{n,yy} - k^2 G_n + (-1)^n F_n (G_1 - G_2) + \frac{Q_{n,y}}{U_n - c} G_n = \delta(y - y') \delta_{n1}, \quad c = \frac{ip}{k} \quad (15)$$

and matching conditions at $y = 0, \pm D$,

$$\left[\frac{G_n}{U_n - c} \right] = 0, \quad [(U_n - c)G_{n,y} - U_{n,y}G_n] = 0. \quad (16)$$

The precise form of G_n is given in appendix B. Because $Q_{n,y} = \beta$ and $U_n = 0$ in $|y| > D$, (15) indicates that G_n consists of the barotropic and baroclinic Rossby waves in these regions [see (B8)]. The numerator of the last term on the lhs of (15) is zero in $|y| < D$, and the critical layer, at which $U_n - c = 0$, is not substantial for G_n .

By inverse Laplace transformation, we have

$$\begin{aligned} \psi_n &= \phi_n e^{ikx} \\ &= \int_0^D G_n[y; y', -ikU_1(y')] q_0(y') e^{ik[x - U_1(y')t]} dy' \\ &+ \text{normal modes.} \end{aligned} \quad (17)$$

Here, the normal modes originate from the poles of G_n at $p = p_m$ ($m = 1, 2, \dots$). The first term corresponds to a continuous spectrum (Pedlosky 1964). The continuous spectrum is associated with the perturbation potential vorticity q_0 , which is advected by the basic flow in $0 < y < D$. Thus, the phase speed of the Rossby waves originated from the continuous spectrum matches with the speed of the basic flow. The continuous spectrum is missing from the solution of a similar analytic model proposed by Talley (1983a,b).

The perturbation attenuates as the contours of the perturbation potential vorticity are zonally elongated by the shear of the basic flow (Fig. 14). If (A5) is satisfied, then the basic flow in the upper layer reaches

a minimum U_m at $|y| = y_m < D$. Then, the solution asymptotes to

$$\begin{aligned} \psi_n &= \sqrt{\frac{\pi}{4kU_{1,yy}(y_m)t}} G_n(y; y_m, -ikU_m) q_0(y_m) e^{ik(x - U_m t)} \\ &+ \text{normal modes} \end{aligned} \quad (18)$$

for large t because contours of the potential vorticity are not sheared at the minimum U_m . It can be shown that the normal modes are neutral in this case because $[Q_n] = [-U_{n,y}] > 0$ at $y = 0, \pm D$ (see Fig. 14). Thus, failing to extract energy from the basic flow, the normal modes cannot radiate energy and are evanescent in $|y| > D$. The baroclinic mode is also evanescent in midlatitudes at the frequencies considered in the present study, $\approx O(10^{-2})$ cpd (Fig. 11). Thus, only the barotropic Rossby waves that match with U_m are radiated. Therefore, the analytic model discussed here captures the basic feature of the Rossby waves in the numerical experiments.

The radiation of the Rossby waves is accompanied by the eddy potential vorticity flux in the upgradient direction of the basic potential vorticity. From the transformed Eulerian mean theory for the zonal-mean flow, the temporal variation of the eddy enstrophy at the discontinuity of the basic potential vorticity at $y = 0, \pm D$ is essential for the eddy potential vorticity flux, because the forcing and dissipation are not explicitly considered here. Similarly, advection of eddy enstrophy, as well as the forcing and dissipation, corresponds to the eddy potential vorticity flux in the time-mean flow. As reported by Holland and Rhines (1980), the eddy enstrophy decreases in the downstream direction of the mean flow in the transient region, from which the Rossby waves are radiated (Figs. 6, 12).

b. Adjustment process of the wave intensity

The rms of the eddy potential vorticity on the $26.3\text{-}\sigma_\theta$ surface for different experiments is compared in Fig. 12. As in Fig. 7, Figs. 12a–d are displayed in the increasing order of the mean potential vorticity of the outflow j_{out} . The intensity of eddy motions along the recirculation, $y \sim \pm 150$ km, increases with the mean potential vorticity of the outflow, and the region of the large rms of eddy potential vorticity along the recirculation is not clear in experiment N5. Thus, the intensity of eddy motions along the recirculation is correlated with that of the Rossby wave radiation, which is consistent with the radiation mechanism proposed in the previous subsection.

In the transient region, where eddies are shed from the jet to the recirculation, the eastward jet is broadened on

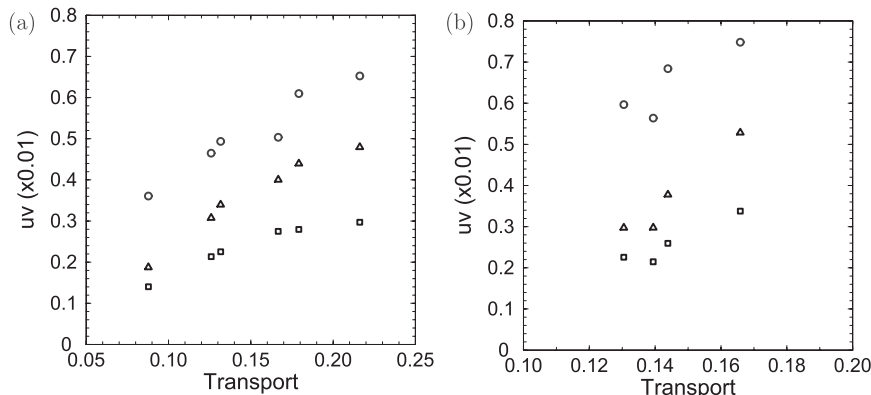


FIG. 15. As in Fig. 10, but for scatterplots of the transport $\Delta\Pi_m$ of the recirculation vs the Reynolds stress $\overline{u'v'}$ integrated in the zonal and vertical directions. Here, $\Delta\Pi_m$ is normalized with $f_0 u_0 l_\beta$.

the $26.3\text{-}\sigma_\theta$ surface. The northern and southern parts of the broadened jet do not directly enter the interior region but rather turn westward and join the recirculation, contributing to the increase in the transport of the recirculation near the transient region (Fig. 6). The transport of the recirculation increases with the mean potential vorticity of the outflow and is correlated with the rms of eddy potential vorticity along the recirculation. In contrast, the maximum rms of the eddy potential vorticity along the jet axis, which corresponds to the source of eddies, does not change significantly in experiments shown in Fig. 12. Thus, the entrainment of eddies into the recirculation is enhanced more significantly by the increase of the mean transport, which affects advection of eddies than by the strengthening of the source in these experiments. Note that the transport on the $26.3\text{-}\sigma_\theta$ surface depends primarily on the width of the recirculation rather than on the speed (not shown). Thus, significant effects on the phase speed of the Rossby waves are not expected.

The maximum transport of the recirculation on the $26.3\text{-}\sigma_\theta$ surface and the intensity of the Rossby waves are compared for all experiments (Fig. 15). Here, in order to estimate the transport of the recirculation, changes in the Bernoulli function across westward flows that flank each side of the eastward flow at $y \sim 0$ are calculated for all x as a measure of the transport of the northern and southern recirculations. This quantity is expressed as $\Delta\overline{\Pi}_1(x)$ and $\Delta\overline{\Pi}_2(x)$ for the southern and northern recirculations, respectively. Then, $\Delta\overline{\Pi}_m = \max[\Delta\overline{\Pi}_1(x) + \Delta\overline{\Pi}_2(x)]$ is adopted as a measure of the maximum transport of the recirculation. The transport of the recirculation and the intensity of the Rossby waves are highly correlated, except for one experiment for $u_0 = 0.8 \text{ m s}^{-1}$ (Fig. 15). Therefore, the potential vorticity of the interior flow, the intensity of the Rossby waves, and the transport of the

recirculation near the surface, change consistently with one another. It is suggested that an optimal value of the transport of the recirculation is selected in order to achieve the balance between the potential vorticity flux by the wave radiation and the difference in the potential vorticity between the jet and interior flow.

5. Summary

The relationship between the Rossby waves and the WBCE was investigated, by conducting numerical experiments with the inflow and outflow boundary conditions. An unstable eastward jet flanked by westward recirculations and a broad interior flow are driven by the inflow and outflow in the western and eastern regions, respectively. We focused on the difference in the potential vorticity between the jet and interior flow. The difference changes with the width of the outflow because the normalized potential vorticity flux j_{out} of the outflow increases with width because of the planetary beta effect.

The effect of the Rossby waves on the mean flow is first examined. The barotropic Rossby waves are radiated from the transient region between the jet and interior regions. The eddy potential vorticity flux due to the radiation of the Rossby waves converges and diverges in the northern and southern parts of the transient region, respectively. The change in the mean potential vorticity along mean streamlines is also examined. The meridional gradient of the mean potential vorticity is weakened too much by the instability of the jet, as compared to that of the interior flow. Here, the term gradient denotes the difference between streamlines. When the jet is broadened in the transient region, the potential vorticity flux by the radiation of the Rossby waves compensates for the difference in the mean

potential vorticity between the interior flow and jet that is modified by the instability. Moreover, as the outflow is broadened and the difference in the mean potential vorticity between the jet and interior flow is increased, the Rossby waves are intensified in order to compensate for the increase in the difference. Thus, it is strongly suggested that the Rossby waves are important in matching a jet, such as the Kuroshio Extension, with the broad interior flow.

Then, the radiation process of the Rossby waves from the jet and recirculation is examined. The intensity of the Rossby waves increases with that of eddies, which are characterized with closed contours of the potential vorticity in the recirculation near the surface. The zonal phase speed of the Rossby waves coincides with the speed of these eddies, which are advected westward by the recirculation. These features are consistent with the argument that the Rossby waves are radiated from eddies in the recirculation. An analytic solution in a two-layer model is also presented as a typical example of this argument. The Rossby waves that appear in this solution correspond to the continuous spectrum rather than the normal modes, which is in contrast to the previous study by Talley (1983a,b). The process that determines the intensity of eddies (i.e., the source of the Rossby waves) is also examined. Eddies are shed from the jet to the recirculation in the transient region. The intensity of eddies increases with the transport of the recirculation near the surface, presumably because of mean advection.

Therefore, the potential vorticity of the interior flow, the intensity of the Rossby waves, and the transport of the recirculation near the surface, change consistently with one another. That is, when the mean potential vorticity of the interior flow increases, the transport of the recirculation increases, the radiation of the Rossby waves is intensified, and the convergence of the eddy potential vorticity flux is strengthened, compensating for the increased difference in the mean potential vorticity between the jet and interior flow. In the present study, the inflow and outflow were fixed in time. The results obtained herein may be extended to a more complex flow, such as a wind-driven circulation forced by decadal oscillating winds, in order to gain more insight into the decadal variability in the North Pacific. This is left for future research.

Acknowledgments. The present study was supported by Grants-in-Aid (21540445, 18549429, and 21540447) for Scientific Research from the Ministry of Education, Science, Sports, and Culture, Japan. The author thanks two anonymous reviewers for their helpful comments.

APPENDIX A

Basic Flow

To approximately represent the meridional distribution of the mean potential vorticity obtained in numerical experiments (Fig. 3), the barotropic and baroclinic components of the basic flow are assumed to be

$$\hat{U}_1 = -\frac{\beta}{2}(y^2 - D^2) - \frac{F_2 \Delta Q}{F}(|y| - D) \quad \text{and} \quad (\text{A1})$$

$$\hat{U}_2 = \frac{\Delta Q \sinh \sqrt{F}(|y| - D)}{\sqrt{F} \cosh \sqrt{F}D} \quad (\text{A2})$$

in $|y| < D$ and absent in $|y| > D$, where $F = F_1 + F_2$. Then, we obtain the basic flow U_n ($n = 1, 2$) and the basic potential vorticity Q_n by using

$$U_1 = \hat{U}_1 + \frac{F_1}{F} \hat{U}_2, \quad (\text{A3})$$

$$U_2 = \hat{U}_1 - \frac{F_2}{F} \hat{U}_2, \quad \text{and} \quad (\text{A4})$$

$$Q_{n,y} = \beta + (-1)^n F_n (U_1 - U_2) - U_{n,yy},$$

respectively. The basic flow in the upper layer U_1 is eastward near $y = 0$ and westward to the north and south of $y = 0$, when

$$\Delta Q_a < \Delta Q < \Delta Q_b \quad (\text{A5})$$

with

$$\Delta Q_a = \frac{\beta DF}{2[F_2 + F_1(\sqrt{FD})^{-1} \tanh \sqrt{FD}]},$$

$$\Delta Q_b = \frac{\beta DF}{F_2 + F_1(\cosh \sqrt{FD})^{-1}}.$$

APPENDIX B

Green's Function

To obtain the Green's functions G_n , a new function $G_n^{(pq)}$ ($p = 1, 2, q = 1, 2$) is considered. The function $G_n^{(pq)}$ is expressed with vertical modes as

$$G_n^{(pq)} = \hat{G}_1^{(pq)} - (-1)^n h_n \hat{G}_2^{(pq)}, \quad h_n = \frac{F_n}{F},$$

and each mode satisfies

$$\left. \begin{aligned} \hat{G}_{n,yy}^{(pq)} - k_n^2 \hat{G}_n^{(pq)} &= [\delta(y - y') - (-1)^p \delta(y + y')] \delta_{nq} \quad \text{at } |y| < D \\ \hat{G}_{n,yy}^{(pq)} - \left(k_n^2 + \frac{\beta}{c}\right) \hat{G}_n^{(pq)} &= 0 \quad \text{at } |y| > D \end{aligned} \right\}, \tag{B1}$$

where

$$k_1 = k, \quad k_2^2 = k^2 + F.$$

Thus, $G_n^{(pq)}$ is forced only in the q th mode in the vertical mode domain and symmetric (antisymmetric) in y for $p = 1$ (2). Then, G_n is expressed as

$$G_n = \frac{h_2}{2} [G_n^{(11)} + G_n^{(21)}] + \frac{1}{2} [G_n^{(12)} + G_n^{(22)}]. \tag{B2}$$

Because $G_n^{(1q)} [G_n^{(2q)}]$ is symmetric (antisymmetric), in the following $G_n^{(pq)}$ is considered only in $y > 0$.

The matching conditions appropriate for $G_n^{(pq)}$ at $y = D$ are

$$[G_n^{(pq)}]_D = 0 \quad \text{and} \tag{B3}$$

$$[G_{n,y}^{(pq)}]_D = -[n' - (-1)^n h_n m] G_n^{(pq)}, \tag{B4}$$

where

$$n'c = \beta D + h_2 \Delta Q, \quad mc = \frac{\Delta Q}{\cosh \sqrt{FD}}$$

correspond to the barotropic and baroclinic components of the relative vorticity by the basic flow, respectively. Matching conditions at $y = 0$ are

$$G_{1,y}^{(1q)} = -\frac{\zeta_0}{V_1 - c} G_1^{(1q)}, \tag{B5}$$

$$G_{2,y}^{(1q)} = 0, \quad \text{and} \tag{B6}$$

$$G_n^{(2q)} = 0, \tag{B7}$$

where

$$\begin{aligned} \zeta_0 &= \Delta Q, \\ V_1 &= \left(-\frac{\beta D}{2} + h_2 \Delta Q\right) D + \frac{h_1 \Delta Q}{\sqrt{F}} \tanh \sqrt{FD} \end{aligned}$$

correspond to the relative vorticity and zonal velocity of the basic flow in the upper layer, respectively. These

matching conditions indicate the interaction between vertical modes.

We first seek $H_n^{(pq)}$ that satisfies the same condition as $\hat{G}_n^{(pq)}$, except that the inhomogeneous condition

$$(\hat{G}_{q,y})_{y'} = 1, \quad (\hat{G}_{q,y})_{-y'} = (-1)^{p-1},$$

which is derived from the first equation in (B1), is replaced by

$$(H_{q,y})_{y'} = (-1)^{p-1} (H_{q,y})_{-y'}.$$

Here and in the following, the superscript (pq) is omitted when it should not be confusing.

The form of H_n is assumed to be

$$H_q(y) = \begin{cases} H_q^-(y) & \text{at } y < y' \\ H_q^+(y) & \text{at } y' < y < D \\ H_q^+(D)e^{-\mu_q(y-D)} & \text{at } D < y \end{cases} \quad \text{and}$$

$$H_r(y) = \begin{cases} H_r^i(y) & \text{at } y < D \\ H_r^i(D)e^{-\mu_r(y-D)} & \text{at } D < y, \end{cases}$$

where $r = 3 - q$ and μ_n satisfies

$$k_n^2 - \mu_n^2 + \frac{\beta}{c} = 0, \quad \arg \mu_n = 0, \frac{\pi}{2}. \tag{B8}$$

Using the matching conditions and introducing

$$\begin{aligned} L_1^{(pq)}(y) &= \frac{1}{k_1} \{[-\nu_1 + h_2 m \gamma^{(pq)}] \sinh k_1(y - D) \\ &\quad + k_1 \cosh k_1(y - D)\} \quad \text{and} \end{aligned} \tag{B9}$$

$$\begin{aligned} L_2^{(pq)}(y) &= \frac{1}{k_2 h_1} \{[-\nu_2 \gamma^{(pq)} + h_1 m] \sinh k_2(y - D) \\ &\quad + k_2 \gamma^{(pq)} \cosh k_2(y - D)\} \end{aligned} \tag{B10}$$

with

$$\nu_1 = \mu_1 - n', \quad \nu_2 = \mu_2 - n' + (h_1 - h_2)m,$$

we have

$$\left. \begin{aligned}
 H_q^+(y) &= L_q(y) \\
 H_r^i(y) &= L_r(y) \\
 H_1^{-(11)}(y) &= \frac{h_2 L_{2,y}(0) \sinh k_1(y - y')}{k_1 \cosh k_1 y'} + \frac{L_1(y') \cosh k_1 y}{\cosh k_1 y'} \\
 H_1^{-(21)}(y) &= \frac{L_1(y') \sinh k_1 y}{\sinh k_1 y'} \\
 H_2^{-(12)}(y) &= \frac{L_{1,y}(0) \sinh k_2(y - y')}{h_2 k_2 \cosh k_2 y'} + \frac{L_2(y') \cosh k_2 y}{\cosh k_2 y'} \\
 H_2^{-(22)}(y) &= \frac{L_2(y') \sinh k_2 y}{\sinh k_2 y'}
 \end{aligned} \right\} \quad (\text{B11})$$

The coefficient γ that appears in L_n is defined as

$$\left. \begin{aligned}
 \gamma^{(11)} &= \frac{h_1 S_1}{R_1}, & \gamma^{(21)} &= \frac{h_1 S_1'}{R_1'} \\
 \frac{1}{\gamma^{(12)}} &= \frac{h_2 S_2}{R_2}, & \frac{1}{\gamma^{(22)}} &= \frac{h_2 S_2'}{R_2'}
 \end{aligned} \right\} \quad (\text{B12})$$

$$\begin{aligned}
 R_q &= \left[\frac{k_q(V_1 - c)}{\zeta_0} \cosh k_q y' - h_r \sinh k_q y' \right] (v_r \cosh k_r D \\
 &+ k_r \sinh k_r D) - \frac{k_q h_q}{k_r} \cosh k_q y' (v_r \sinh k_r D \\
 &+ k_r \cosh k_r D) - h_q h_r m \sinh k_q (D - y'),
 \end{aligned}$$

$$\begin{aligned}
 S_q &= \left[\frac{k_q(V_1 - c)}{\zeta_0} \cosh k_q y' - h_r \sinh k_q y' \right] m \cosh k_r D \\
 &- \frac{k_q h_q}{k_r} \cosh k_q y' m \sinh k_r D - [v_q \sinh k_q (D - y') \\
 &+ k_q \cosh k_q (D - y')],
 \end{aligned}$$

$$R'_q = v_r \sinh k_r D + k_r \cosh k_r D, \text{ and}$$

$$S'_q = m \sinh k_r D.$$

Then, we have

$$\left. \begin{aligned}
 \hat{G}_q(y) &= \frac{H_q(y)}{[H_{q,y}]_{y'}} \\
 \hat{G}_r(y) &= \frac{H_r(y)}{[H_{r,y}]_{y'}}
 \end{aligned} \right\} \quad (\text{B13})$$

and from (B11),

$$\left. \begin{aligned}
 [H_{1,y}^{(11)}]_{y'} &= \frac{1}{\cosh k_1 y'} [L_{1,y}(0) - h_2 L_{2,y}(0)] \\
 [H_{1,y}^{(21)}]_{y'} &= -\frac{k_1 L_1(0)}{\sinh k_1 y'} \\
 [H_{2,y}^{(12)}]_{y'} &= \frac{1}{\cosh k_2 y'} \left[L_{2,y}(0) - \frac{1}{h_2} L_{1,y}(0) \right] \\
 [H_{2,y}^{(22)}]_{y'} &= -\frac{k_2 L_2(0)}{\sinh k_2 y'}
 \end{aligned} \right\} \quad (\text{B14})$$

REFERENCES

Boyer, T. P., C. Stephens, J. I. Antonov, M. E. Conkright, R. A. Locarnini, T. D. O'Brien, and H. E. Garcia, 2002: *Salinity*. Vol. 2, *World Ocean Atlas 2001*, NOAA Atlas NESDIS 50, 165 pp.

Cessi, P., 1991: Laminar separation of colliding western boundary currents. *J. Mar. Res.*, **49**, 697–717.

—, R. V. Condie, and W. R. Young, 1990: Dissipative dynamics of western boundary currents. *J. Mar. Res.*, **48**, 677–700.

Ducet, N., and P. Y. L. Taron, 2001: A comparison of surface eddy kinetic energy and Reynolds stresses in the Gulf Stream and the Kuroshio Current systems from merged TOPEX/Poseidon and ERS-1/2 altimetric data. *J. Geophys. Res.*, **106**, 16 603–16 622.

Fox-Kemper, B., and J. Pedlosky, 2004: Wind-driven barotropic gyre. Part I: Circulation control by eddy vorticity fluxes to an enhanced removal region. *J. Mar. Res.*, **62**, 169–193.

Haidvogel, D. B., and P. B. Rhines, 1983: Waves and circulation driven by oscillatory winds in an idealized ocean basin. *Geophys. Astrophys. Fluid Dyn.*, **25**, 1–63.

—, H. G. Arango, K. Hedstrom, A. Beckmann, P. Malanotte-Rizzoli, and A. F. Shchepetkin, 2000: Model evaluation experiments in the North Atlantic Basin: Simulations in nonlinear terrain-following coordinates. *Dyn. Atmos. Oceans*, **32**, 239–281.

Hogg, N. G., 1981: Topographic waves along 70 W on the Continental Rise. *J. Mar. Res.*, **39**, 627–649.

—, 1988: Stochastic wave radiation by the Gulf Stream. *J. Phys. Oceanogr.*, **18**, 1687–1701.

Holland, W. R., 1978: The role of mesoscale eddies in the general circulation of the ocean—Numerical experiments using a wind-driven quasi-geostrophic model. *J. Phys. Oceanogr.*, **8**, 363–392.

—, and P. B. Rhines, 1980: An example of eddy-induced ocean circulation. *J. Phys. Oceanogr.*, **10**, 1010–1031.

- Imawaki, S., and Coauthors, 1997: Time series of the Kuroshio transport from field observations and altimetry data. *International WOCE Newsletter*, No. 25, WOCE International Project Office, Southampton, United Kingdom, 15–18.
- , and Coauthors, 2001: Satellite altimeter monitoring the Kuroshio transport south of Japan. *Geophys. Res. Lett.*, **28**, 17–20.
- Jayne, S. R., and N. G. Hogg, 1999: On recirculation forced by an unstable jet. *J. Phys. Oceanogr.*, **29**, 2711–2718.
- , —, and P. Malanotte-Rizzoli, 1996: Recirculation gyres forced by a beta-plane jet. *J. Phys. Oceanogr.*, **26**, 492–504.
- Malanotte-Rizzoli, P., N. G. Hogg, and R. E. Young, 1995: Stochastic radiation by the Gulf Stream: Numerical experiments. *Deep-Sea Res.*, **42**, 389–423.
- Mizuta, G., 2009: Rossby wave radiation from an eastward jet and its recirculations. *J. Mar. Res.*, **67**, 185–212.
- , and N. G. Hogg, 2004: Structure of the circulation induced by a shoaling topographic wave. *J. Phys. Oceanogr.*, **34**, 1793–1810.
- Munk, W. H., 1950: On the wind-driven ocean circulation. *J. Meteor.*, **7**, 79–93.
- Pedlosky, J., 1964: An initial value problem in the theory of baroclinic instability. *Tellus*, **16**, 12–17.
- , 1987: *Geophysical Fluid Dynamics*. 2nd ed. Springer-Verlag, 710 pp.
- Qiu, B., and S. Chen, 2005: Variability of the Kuroshio Extension jet, recirculation gyre, and mesoscale eddies on decadal time scales. *J. Phys. Oceanogr.*, **35**, 2090–2103.
- , and —, 2010: Eddy-mean flow interaction in the decadal modulating Kuroshio Extension system. *Deep-Sea Res. II*, **57**, 1098–1110.
- Stephens, C., J. I. Antonov, T. P. Boyer, M. E. Conkright, R. A. Locarnini, T. D. O'Brien, and H. E. Garcia, 2002: *Temperature*. Vol. 1, *World Ocean Atlas 2001*, NOAA Atlas NESDIS 49, 167 pp.
- Stommel, H., 1948: The westward intensification of wind-driven ocean currents. *Trans. Amer. Geophys. Union*, **29**, 202–206.
- Taguchi, B., S. P. Xie, H. Mitsudera, and A. Kubokawa, 2005: Response of the Kuroshio Extension to Rossby waves associated with the 1970s climate regime shift in a high-resolution ocean model. *J. Climate*, **18**, 2979–2995.
- , —, N. Schneider, M. Nonaka, H. Sasaki, and Y. Sasai, 2007: Decadal variability of the Kuroshio Extension: Observations and an eddy-resolving model hindcast. *J. Climate*, **20**, 2357–2377.
- Talley, L. D., 1983a: Radiating barotropic instability. *J. Phys. Oceanogr.*, **13**, 972–987.
- , 1983b: Radiating instabilities of thin baroclinic jets. *J. Phys. Oceanogr.*, **13**, 2161–2181.
- Thompson, R., 1977: Observations of Rossby waves near site D. *Prog. Oceanogr.*, **7**, 1–28.
- Waterman, S., and S. R. Jayne, 2011: Eddy-mean flow interactions in the along-stream development of a western boundary current jet: An idealized model study. *J. Phys. Oceanogr.*, **41**, 682–707.